



Comparative study of nanoparticle uptake and impact in murine lung, liver and kidney tissue slices

Roberta Bartucci, Abhimata Paramanandana, Ykelien L. Boersma, Peter Olinga & Anna Salvati

To cite this article: Roberta Bartucci, Abhimata Paramanandana, Ykelien L. Boersma, Peter Olinga & Anna Salvati (2020) Comparative study of nanoparticle uptake and impact in murine lung, liver and kidney tissue slices, *Nanotoxicology*, 14:6, 847-865, DOI: [10.1080/17435390.2020.1771785](https://doi.org/10.1080/17435390.2020.1771785)

To link to this article: <https://doi.org/10.1080/17435390.2020.1771785>



© 2020 The Author(s). Published by Informa UK Limited, trading as Taylor & Francis Group.



[View supplementary material](#)



Published online: 13 Jun 2020.



[Submit your article to this journal](#)



Article views: 2263



[View related articles](#)



[View Crossmark data](#)



Citing articles: 5 [View citing articles](#)

ARTICLE



Comparative study of nanoparticle uptake and impact in murine lung, liver and kidney tissue slices

Roberta Bartucci^{a,b,c}, Abhimata Paramanandana^a, Ykelien L. Boersma^b, Peter Olinga^c and Anna Salvati^a

^aDepartment of Pharmacokinetics, Toxicology and Targeting, Groningen Research Institute of Pharmacy, University of Groningen, Groningen, The Netherlands; ^bDepartment of Chemical and Pharmaceutical Biology, Groningen Research Institute of Pharmacy, University of Groningen, Groningen, The Netherlands; ^cDepartment of Pharmaceutical Technology and Biopharmacy, Groningen Research Institute of Pharmacy, University of Groningen, Groningen, The Netherlands

ABSTRACT

To determine responses to nanoparticles in a more comprehensive way, current efforts in nano-safety aim at combining the analysis of multiple endpoints and comparing outcomes in different models. To this end, here we used tissue slices from mice as 3D *ex vivo* models and performed for the first time a comparative study of uptake and impact in liver, lung, and kidney slices exposed under the same conditions to silica, carboxylated and amino-modified polystyrene. In all organs, only exposure to amino-modified polystyrene induced toxicity, with stronger effects in kidneys and lungs. Uptake and distribution studies by confocal microscopy confirmed nanoparticle uptake in all slices, and, in line with what observed *in vivo*, preferential accumulation in the macrophages. However, uptake levels in kidneys were minimal, despite the strong impact observed when exposed to the amino-modified polystyrene. On the contrary, nanoparticle uptake and accumulation in macrophages were particularly evident in lung slices. Thus, tissue digestion was used to recover all cells from lung slices at different exposure times and to determine by flow cytometry detailed uptake kinetics in lung macrophages and all other cells, confirming higher uptake by the macrophages. Finally, the expression levels of a panel of targets involved in inflammation and macrophage polarization were measured to determine potential effects induced in lung and liver tissue. Overall, this comparative study allowed us to determine uptake and impact of nanoparticles in real tissue and identify important differences in outcomes in the organs in which nanoparticles distribute.

ARTICLE HISTORY

Received 4 March 2020
Revised 12 May 2020
Accepted 15 May 2020

KEYWORDS

Tissue slices; *ex vivo*;
advanced models;
fluorescence imaging;
flow cytometry



Introduction


Whether nanomaterial accumulation results from administration of nanomedicines designed to deliver drugs for therapeutic purposes, or from unintentional exposure to nanoparticles used for other nanotechnology applications, or simply from air pollution, it is important to determine potential effects induced by nanoparticles in the organs in which they distribute (Oberdörster, Oberdörster, and Oberdörster 2005; Nel et al. 2006).

Unintentional exposure to nanomaterials can occur mainly through inhalation, ingestion, and dermal contact. Additionally, cells and organs may be directly exposed to nanomaterials, when for

instance surgical implants including nanoparticles are used (Armstead and Li 2016).

Among the different routes, pulmonary exposure is one of the most studied route in nanosafety, given the large presence of particulates in the air and the continuous exposure (Krug 2014). It has been established that after inhalation, two thirds of the nanomaterials are cleared via mucociliary action and one third reaches the deepest regions of the lungs (true for nanoparticles, but not for microparticles (Kreyling et al. 2013; Riediker et al. 2019)). In the alveoli, nanoparticles usually have been observed to accumulate in the alveolar macrophages, and/or in the epithelial cells (specifically, in type I epithelial cells (Thorley et al. 2014)).

CONTACT Anna Salvati  a.salvati@rug.nl 

 Supplemental data for this article can be accessed [here](#).

© 2020 The Author(s). Published by Informa UK Limited, trading as Taylor & Francis Group.

This is an Open Access article distributed under the terms of the Creative Commons Attribution-NonCommercial-NoDerivatives License (<http://creativecommons.org/licenses/by-nc-nd/4.0/>), which permits non-commercial re-use, distribution, and reproduction in any medium, provided the original work is properly cited, and is not altered, transformed, or built upon in any way.

Translocation in the interstitial space has also been observed, followed by clearance via the lymphatic system (Bierkandt et al. 2018), sequestration by interstitial macrophages, and/or translocation to the systemic circulation (Oberdörster, Oberdörster, and Oberdörster 2005; Choi et al. 2010; Kreyling et al. 2013; Riediker et al. 2019).

Indeed, not only after inhalation, but regardless of the route of exposure (or administration in the case of nanomedicines), distribution studies show that nanomaterials usually can reach to some extent the blood stream. Once in the blood, they tend to accumulate into secondary organs, with kidneys and liver usually among the most relevant ones (De Jong et al. 2008; Choi et al. 2010; Schleh et al. 2012). Indeed, the liver is also a well-known barrier for drug delivery (accumulation in the liver sometimes can be even higher than at the intended target site, for instance into a tumor (Wilhelm et al. 2016)). Within the liver, nanomaterials mainly accumulate in the Kupffer cells (Tsoi et al. 2016), the resident liver macrophages, followed by liver sinusoidal endothelial cells, hepatic stellate cells and only in lower percentage in the hepatocytes (Bartneck, Warzecha, and Tacke 2014; Park et al. 2016; Haute and Berlin 2017). Together with the liver, the kidneys also have a central role in the filtration and excretion of nanomaterials (Longmire, Choyke, and Kobayashi 2008; Du, Yu, and Zheng 2018). Size (because of the fenestrae in the endothelium (Choi et al. 2011)), charge (because of the capillary wall of the glomeruli), and shape (because of the glomeruli basement membrane) carefully orchestrate the fate of nanomaterials in the renal environment (Liu et al. 2013).

With this in mind, in this study we aimed at comparing nanoparticle impact in lungs, liver, and kidneys, selected as three of the major organs for nanosafety assessment (Olinga and Schuppan 2013; Sauer et al. 2014; Stribos et al. 2017).

Many efforts within the nanosafety field are currently focusing on the implementation of advanced *in vitro* models, such as co-cultures, organoids, and organ-on-a-chip devices to investigate the behavior and impact of nanomaterials in more complex systems than simple cell cultures (Huh, Hamilton, and Ingber 2011; Klein et al. 2013; Mahto et al. 2015; Wick et al. 2015; Burden et al. 2017; Fadeel et al. 2018). Advanced models should resemble specific

features of the different organs in which nanoparticles accumulate, including their environment, cell architecture, and composition. By mimicking the complexity of the *in vivo* environment, such models could help to reduce the need for animal studies, in accordance with the 3 R's principle (reduction, replacement, and refinement) and, ideally, also to reduce the gap between outcomes observed in animal models and in humans.

Within this context, we used precision-cut tissue slices (Parrish, Gandolfi, and Brendel 1995; de Graaf et al. 2010) as an advanced 3D *ex vivo* model to compare uptake, distribution, and impact of nanoparticles in lungs, liver, and kidneys.

Although nanoparticle studies using tissue slices have mainly been focused on lung slices (Paranjpe et al. 2013; Ahlberg et al. 2014; Sauer et al. 2014; Neuhaus et al. 2018; Osman et al. 2018), to the best of our knowledge, there are no studies yet in literature where a direct comparison of nanoparticle impact on tissue slices from different organs has been made.

To this end, we exposed tissue slices from the different organs to a panel of model nanoparticles already well characterized, including 50 nm silica (SiO₂), and carboxylated and amino-modified polystyrene nanoparticles of different sizes and charge (40 and 200 nm PS-COOH, and 50 nm PS-NH₂, negatively and positively charged, respectively). SiO₂ and PS-COOH nanoparticles are usually considered non-toxic (Barnes et al. 2008; Shapero et al. 2011; Loos et al. 2014). However, some studies have reported inflammatory responses and toxicity following exposure to silica nanoparticles (Park et al. 2011; Kusaka et al. 2014; Kim et al. 2015). The PS-NH₂ nanoparticles, instead, are a common model for toxicity induced by positive charges (Xia et al. 2008; Wang et al. 2013).

Then, viability tests and morphological analysis of the tissue were used to determine the impact of the different nanoparticles and compare the outcomes in the lung, liver, and kidney tissue slices. This was coupled to fluorescence imaging and immunostaining, which were used to determine nanoparticle uptake into the tissue and compare uptake efficiency and distribution in the different organs. Finally, additional studies were performed on selected organs and conditions to confirm and investigate in more detail some of the outcomes

observed. These included tissue digestion and flow cytometry on lung slices exposed to the 40 nm PS-COOH for a quantitative analysis of nanoparticle uptake kinetics in different cell types in the lungs, and the gene expression analysis of a panel of markers involved in inflammation and macrophage polarization in the lungs and the liver.

The comparison of outcomes on tissue slices from different organs exposed to the same panel of nanoparticles is a powerful tool to define common features and differences in the response of different tissues to nanomaterials.

Materials and methods

Animals

Male and female C57BL/6J mice (6–10 weeks old) were kept in a temperature- and humidity-controlled room with a 12-h light/dark cycle with food and water *ad libitum*. Mice were housed in the animal facility for at least one week before starting the experiments. Mice were sacrificed under isoflurane/O₂ anesthesia (Nicholas Piramil, London, UK) and their organs were harvested. Liver and kidneys were directly extracted, whereas the lungs were inflated *in situ* with liquefied and pre-warmed (37 °C) support medium containing 1.5% low-gelling-temperature agarose type VII (Sigma-Aldrich, Zwijndrecht, The Netherlands) in 0.9% NaCl (Merck, Darmstadt, Germany) to prevent tissue collapse. All experiments were approved by the Animal Ethical Committee of the University of Groningen.

Preparation of precision-cut tissue slices

Precision-cut tissue slices were prepared as described earlier (de Graaf et al. 2010). Briefly, liver and lung cores were prepared by using biopsy punches with a 5 mm diameter cylindrical tip and afterwards cut into slices with Krumdieck Tissue Slicer MD6000 (Alabama R&D, Munford, TN, USA). Due to their small size, the kidneys were positioned entirely in the core holder of the Krumdieck tissue slicer. The slicer was filled with ice-cold Krebs–Henseleit buffer supplemented with 25 mM D-glucose (Merck, Darmstadt, Germany), 25 mM NaHCO₃ (Merck, Darmstadt, Germany), and 10 mM Hepes (MP Biomedicals GmbH, Germany), and saturated with a mixture of 95% oxygen and 5% CO₂.

Liver and kidney slices were about 200–250 µm thick and their weight was of around 5 mg, whereas the lung slices were 250–300 µm thick and their weight (which includes the weight of the agarose in the section) was of roughly 6 mg. After the slicing procedure, precision-cut tissue slices prepared from the three organs were preserved in University of Wisconsin organ preservation solution (UW) (DuPont Critical Care, Waukegan, IL, USA) on ice until further use.

Pre-incubation of precision-cut tissue slices

To remove the UW solution before the experimental procedure, slices were transferred to a petri dish containing William's Medium E + GlutaMAX medium (WME, with L-glutamine, Life Technologies, Bleiswijk, The Netherlands) enriched with 25 mM D-glucose and 50 µg/mL gentamycin (Life Technologies, Bleiswijk, The Netherlands). Afterwards, the tissue slices were incubated in 1.3 mL pre-warmed and oxygenated culture medium at 37 °C under 5% CO₂ and 80% O₂, while being gently shaken (90 cycles per min). The liver slice medium was composed of William's Medium E + GlutaMAX (Life Technologies, Bleiswijk, The Netherlands) supplemented with 25 mM D-Glucose (Sigma-Aldrich, Zwijndrecht, The Netherlands), 50 µg/mL gentamycin (Life Technologies, Bleiswijk, The Netherlands), and 5% v/v Fetal Bovine Serum (FBS, Gibco from Thermo Fisher Scientific, Bleiswijk, The Netherlands). The kidney slice medium was composed of William's Medium E + GlutaMAX supplemented with 25 mM D-Glucose, 10 µg/mL ciprofloxacin (Fresenius Kabi, Zeist, The Netherlands), and 5% v/v Fetal Bovine Serum (FBS, Gibco from ThermoFisher Scientific, Bleiswijk, The Netherlands). The lung slice medium was composed of William's Medium E + GlutaMAX supplemented with 25 mM D-Glucose, 50 µg/mL gentamycin, 100 U/mL penicillin-streptomycin (Life Technologies, Bleiswijk, The Netherlands) and 5% v/v Fetal Bovine Serum (FBS, Gibco from Thermo Fisher Scientific, Bleiswijk, The Netherlands). Prior to exposure to the nanoparticles, tissue slices were pre-incubated for 3 h in these conditions to restore tissue function and to reduce the presence of cell debris and eventual dead cells on the edge of the slices after the cutting procedure.

Dynamic light scattering measurement

Dark-red labeled 40 nm carboxylated-modified polystyrene nanoparticles (PS-COOH, maximum excitation at 660 nm and maximum emission at 680 nm) were purchased from Thermo Fisher Scientific (Bleiswijk, The Netherlands) and unlabeled 50 nm amino-modified polystyrene nanoparticles (PS-NH₂) were purchased from Bang Laboratories, Polysciences Europe GMBH, Hirschberg an der Bergstrasse, Germany). Plain silica of 50 nm (SiO₂, excitation 569 nm and emission 589 nm) were purchased from Kisker (Leiden, The Netherlands). Orange labeled 200 nm carboxylated-modified polystyrene nanoparticles (PS-COOH, excitation 540 nm and emission 560 nm) were purchased from Thermo Fisher Scientific (Bleiswijk, The Netherlands). Nanoparticle dispersions were characterized by Dynamic Light Scattering (DLS, Malvern Zetasizer). For this purpose, the nanoparticles were dispersed at a final concentration of 100 µg/mL in Milli-Q water and WME supplemented with 5% v/v FBS and the obtained dispersions immediately measured by DLS. The nanoparticle dispersions in WME supplemented with 5% FBS were also measured after 24 h of incubation in the conditions used for tissue maintenance described above. The results are shown as the average of three separate measurements from one representative experiment and each measurement included 10 runs of 10 sec.

Exposure to nanoparticles

After 3 h pre-incubation, tissue slices were transferred to pre-warmed (37 °C) and pre-saturated (80% O₂/5% CO₂) wells containing the nanoparticle dispersions at different doses in WME medium supplemented with 5% v/v FBS. The slices were collected after 48 h and washed for 3 h in fresh WME medium supplemented with 5% v/v FBS without nanoparticles, to reduce the presence of potential nanoparticles adsorbed on the edge of the sections.

ATP assay for tissue viability

The ATP assay was used to measure tissue viability: the ATP content (pmol) was normalized by the total protein content (µg). Then, the results obtained in treated slices were divided by the results in untreated control slices not exposed to the nanoparticles. For each condition, three slices of the same

animal were used, and the average and standard deviation calculated. The results obtained in one representative experiment are shown in [Supplementary Figures S3–S5](#). The three slices were pooled together after exposure. Slices were quickly washed twice with medium and once with PBS to remove potential nanoparticles adsorbed on the edge of the tissue slice. Next, each slice was collected in 1 mL of sonication solution containing 70% v/v ethanol and 2 mM EDTA (pH 10.9), snap frozen in liquid nitrogen, and stored at –80 °C until further analysis. To determine the viability of the slices, ATP levels were measured as described previously (Starokozhko et al. 2015). In brief, samples were thawed slowly on melting ice, homogenized for 45 s using a Mini-BeadBeater 24 (Biospec Products), and centrifuged at 16 100 g for 5 min at 4 °C. The supernatant was diluted ten times in 0.1 M Tris HCl buffer (pH 7.8) containing 2 mM EDTA, and the ATP content was determined using the ATP Bioluminescence Assay Kit CLS II (Roche Diagnostics, Mannheim, Germany) in a black 96-well plate Lucyl luminometer (Anthos) following the manufacturer instructions. After centrifugation the pellet was kept at 37 °C for determination of the protein content of the slice. Next, the pellet was reconstituted in 200 µL of 5 M NaOH for 30 min at 37 °C. After dilution with 800 µL Milli-Q water, the protein content was measured according to the Lowry assay using a Bio-Rad DC Protein Assay (Bio-Rad, Munich, Germany) with bovine serum albumin as a standard to build a calibration curve. The plate was kept in the dark for 15 min, then the absorbance at 650 nm was measured. Experiments were repeated multiple times, and the data show the mean and standard error of the mean (SEM) of the results obtained in 3–9 independent experiments. Each symbol represents the results obtained in an independent experiment.

Preparation of cryo- and paraffin- sections of tissue slices

To prepare cryoblocks, tissue slices were embedded in KP-cryocompound (Klinipath BV, Olen, Belgium) and frozen in 2-methylbutane (Sigma-Aldrich, Zwijndrecht, The Netherlands) on dry ice after being washed for 3 h in fresh medium and quickly with PBS. Then, sections of 4 µm thickness were prepared using a CryoStar NX70 cryostat (Thermo Fisher

Scientific, Bleiswijk, The Netherlands) and were cut perpendicular to the surface of the slice. For paraffin embedding, tissue slices were collected and fixed in 4% formaldehyde in PBS solution for 24 h at 4 °C and stored until analysis in 70% ethanol at 4 °C. After dehydration in alcohol and xylene, the slices were embedded in paraffin and sectioned (4 µm thick) perpendicular to the surface of the slice using a Leica Reichert-Jung 2040 Autocut Microtome.

Immunofluorescence staining of cryo-sections

Cryo-sections were cut and stained the same day. Sections were dried for 30 min at room temperature, fixed with 4% formaldehyde (Klinipath BV, Olen, Belgium) for 15 min at room temperature and permeabilized with 0.2% triton X-100 (Sigma-Aldrich, Zwijndrecht, The Netherlands) for 15 min. Next, slices were incubated with 50 µL of a primary antibody solution for 60 min at room temperature followed by incubation with 50 µL of a secondary antibody solution for another 60 min at room temperature in the darkness. Both antibodies were diluted in 5% normal mouse serum (NMS) in PBS to block nonspecific binding. 4',6-diamidino-2-phenylindole (DAPI, 1 µg/mL) was applied for 5 min to stain the nuclei and finally the slides were mounted with a glass cover slip using MOWIOL 4-88 (Merck Millipore, Burlington, MA, USA). A rat anti-murine CD68 antibody was used to stain macrophages in all the tissue slices (Bio-Rad, Munich, Germany 1:50), then a goat anti-rat Alexa Fluor 555 or Alexa Fluor 488 (Thermo Fisher Scientific, Bleiswijk, The Netherlands, 1:200) secondary fluorescently labeled antibodies were used. Images were acquired on a Leica SP8 confocal microscope, using 20X and 40X objectives, with a 405 nm laser for DAPI excitation, a 488 nm laser for Alexa Fluor 488, a 555 nm laser for Alexa Fluor 555 and SiO₂ nanoparticles, and a 638 nm laser for the dark-red nanoparticles. To obtain images of the entire slice section, multiple adjacent images were acquired in the same z-plane using the same settings, then individual TIFF files were merged together using the 2D stitching plugin of the Fiji-ImageJ software.

Morphological assessment on paraffin sections

Paraffin embedded sections were deparaffinized, rehydrated, and stained with hematoxylin and eosin (H&E). Briefly, the paraffin sections were deparaffinized and rehydrated with decreasing strengths of ethanol (100% to 50%). Then, sections were immersed in hematoxylin (Klinipath BV, Olen, Belgium) for 10 min. Afterwards, sections were dehydrated in baths of increasing strengths of ethanol (50% to 100%) and immersed for 2 min in eosin (Klinipath). Finally, slides were mounted with glass cover slips using DePeX (Serva Electrophoresis GmbH, Germany). Sections were scanned with a C9600 NanoZoomer (Hamamatsu Photonics).

Quantitative real-time PCR

For each experimental condition, three slices were collected in a 1 mL tube for liver tissue and six slices for lung tissue, snap frozen in liquid nitrogen and kept at −80 °C until further use. The total RNA was isolated from tissue slices using Maxwell LEV simply RNA Cells/Tissue Kit (Promega, Leiden, The Netherlands) following the manufacturer's instructions. Afterwards, the RNA concentration was measured using a NanoDrop ND-100 spectrophotometer (NanoDrop Technologies). Two µg of mRNA were reverse-transcribed into cDNA using a Reverse Transcription System (Promega, Leiden, The Netherlands); the following cycle was used: 20 °C for 10 min, 42 °C for 30 min, 20 °C for 12 min, 99 °C for 5 min and 20 °C for 5 min. Next, transcription levels were measured by quantitative Real Time PCR (SensiMix SYBR kit, Bioline, London, UK) in an ABI7900HT sequence detection system (Applied Biosystems) from 20 ng of cDNA. The primers used included:

β-actin (FW) 5'-ATCGTGCGTGACATCAAAGA
(RV) 5'-ATGCCACAGGATTCCATACC
IL-1β (FW) 5'-GCCAAGACAGGTCGCTCAGGG
(RV) 5'-CCCCCACACGTTGACAGCTAGG
IL-6 (FW) 5'-TGATGCTGGTGACAACCACGGC
(RV) 5'-TAAGCCTCCGACTTGTGAAGTGGTA
IL-10 (FW) 5'-ATAACTGCACCCACTTCCCACT
(RV) 5'-CCCAAGTAACCCCTTAAAGTCCTGC
Ym-1 (FW) 5'-ACTTTGATGGCCTCAACCTG
(RV) 5'-AATGATTCTCTCCTGTGG

MHCII (FW) 5'-TCCAGATGCCAACGTGGCCC
(RV) 5'-TGCGGAAGAGGTGATCGTCCC

The Ct values were obtained using the SDS 2.4 software (Applied Biosystems). For each gene, three replicate wells were prepared and the average Ct value was calculated. Then, the ΔCt was calculated ($\text{Ct}_{\text{gene}} - \text{Ct}_{\text{housekeeping gene}}$). Then, the $\Delta\Delta\text{Ct}$ was calculated as $\Delta\text{Ct} - \text{Ct}_{\text{negative control}}$, and finally the fold induction of $\Delta\Delta\text{Ct}$ as $2^{-\Delta\Delta\text{Ct}}$, as shown in Figure 6.

Tissue digestion and flow cytometry analysis

The Mouse tissue dissociation kit from Miltenyi Biotec (Bergisch Gladbach, Germany) was used for the enzymatic digestion of murine lung slices. For each condition, 6 lung slices were prepared and, after exposure to nanoparticles, were washed for 3 h with WME medium supplemented with 5% v/v FBS. Then, the slices were pooled together in a 50 mL tube containing the dissociation mix, which was prepared as follows: 100 μL Enzyme D solution, 50 μL Enzyme R solution, and 10 μL Enzyme A solution in 5 mL WME medium supplemented with 5% v/v FBS. The samples were incubated for 15 min at 37°C in a water bath with shaking and every 5 min samples were gently resuspended. After digestion for 15 min, the lung tissue was gently smashed and then passed through a 70 μm nylon strainer (BD Bioscience, Drachten, The Netherlands) to obtain single cell suspensions, and the filters were washed with additional 5 mL of medium. Approximately, 1×10^6 cells per sample were recovered. Cells were centrifuged and resuspended twice in sterile PBS. Then, to discriminate live and dead cells, samples were incubated with the Fixable Viability Dye eFluo 450 (eBioscience, Thermo Fisher, Landsmeer, The Netherlands 1:2000 dilution) in serum/protein-free PBS for 30 min on ice in the dark. After, cells were washed twice with a solution of 2% v/v FBS, 5 mM EDTA in PBS (PFE buffer) and incubated with Fix/Perm buffer (eBioscience) for 30 min on ice. Next, cells were washed with Perm-buffer (eBioscience, Thermo Fisher, Landsmeer, The Netherlands) once. The isolated cells were incubated with a PE/Cy7 anti-mouse CD68 antibody (Biolegend, London, UK 1:100) for 30 min on ice in the dark to stain the macrophages. Finally, cells

were washed twice with Perm-buffer, resuspended in PFE buffer, and immediately measured using a Cytoflex S Flow Cytometer (Beckman Coulter, Woerden, The Netherlands) with 405 nm (for live/dead staining), 488 nm (for macrophages) and 630 nm (for nanoparticles) lasers. Data were analyzed using Flowjo software (Flowjo, LLC). Dead cells were excluded from the analysis by setting gates in side scattering versus FL5:PB450 double scatter plots. Cell doublets were excluded by setting gates in the forward scattering area versus forward scattering height double scatter plots. The gating strategy is illustrated in [Supplementary Figure S6](#). For each sample, 25 000–50 000 cells were acquired. [Figure 5](#) shows the average and standard deviation of the results obtained in three independent experiments (with the exception of the 16 h sample which was included only in two experiments).

Statistics

All experiments were carried out three times or more (≥ 3 animals) and each experiment included three slices for each condition. For mRNA expression, data are presented as the mean and standard error of the mean of the $2^{-\Delta\Delta\text{Ct}}$ values obtained in three independent experiments. Kruskal–Wallis statistic followed by Dunnett's multiple comparisons test were performed on ΔCt values using GraphPad 5.0.

Results

Prior to exposure to tissue slices, the nanoparticle dispersions in Milli-Q water and WME medium supplemented with 5% fetal bovine serum (FBS) v/v (WME + 5% FBS) were characterized by Dynamic Light Scattering (DLS; [Supplementary Figure S1](#) and [Table S1](#)).

The DLS results ([Supplementary Table S1](#) and [Figure S1](#)) showed that in the case of the 40 and 200 nm PS-COOH, as well as of the 50 nm SiO₂ nanoparticles homogenous dispersions were obtained both in Milli-Q water and WME + 5% FBS. However, for the PS-NH₂ polystyrene homogenous dispersions could be obtained only in Milli-Q water, whereas agglomeration was observed in WME + 5% FBS.

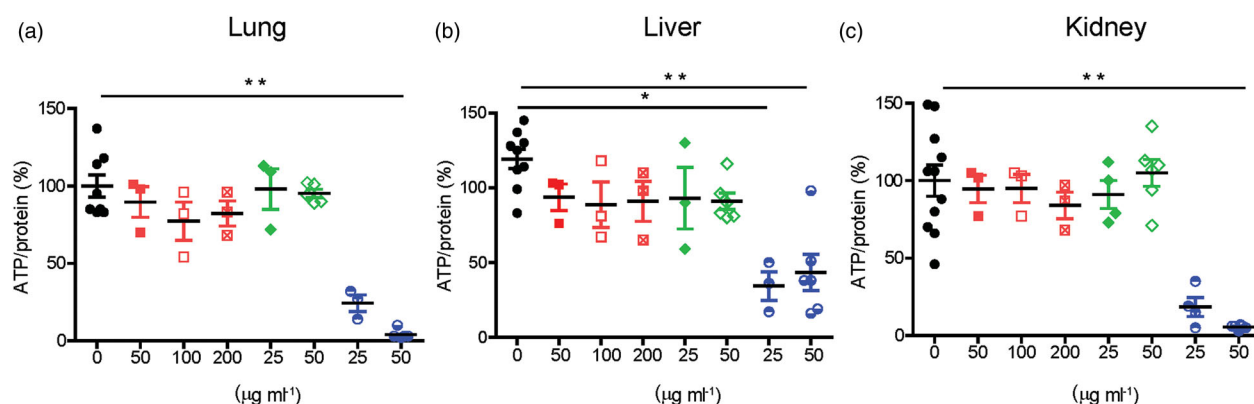


Figure 1. Viability of murine lung, liver, and kidney slices exposed to SiO_2 , PS-COOH, and PS-NH₂ nanoparticles. Lung (a), liver (b), and kidney (c) slices were exposed for 48 h to increasing doses of 50 nm SiO_2 (red), 40 nm PS-COOH (green), and 50 nm PS-NH₂ (blue) in medium supplemented with 5% FBS (For interpretation of the references to colours in this legend, please refer to the web version of this article.). Viability is expressed as the percentage (%) of ATP normalized by total protein amount (pmol/ μg). The results on liver slices exposed to the two polystyrene nanoparticles are reproduced from (Bartucci et al. 2020). Kruskal–Wallis statistic followed by Dunnett’s multiple comparisons test was performed. * = $p \leq 0.05$; ** $p \leq 0.01$. The data show the mean and standard error of the mean (SEM) of the results obtained in 3 to 11 independent experiments. Every dot represents the result of an independent experiment. For each experiment, the results of the treated slices are normalized by the results obtained in untreated control slices from the same animal (0 $\mu\text{g}/\text{mL}$ nanoparticles). For each condition three slices of the same animal were used, and the average and SEM were calculated. The results obtained in one representative experiment are shown in Supplementary Figures S3–S5.

Next, murine slices of liver, lung, and kidney were exposed to increasing doses of PS-COOH, PS-NH₂, and SiO_2 nanoparticles in WME + 5% FBS up to 48 h. Tissue viability was determined (Figure 1 and Supplementary Figures S2–S5 for initial tests at 100 $\mu\text{g}/\text{mL}$ PS-NH₂ and results in individual experiments) and tissue sections were imaged for morphological assessment (Figure 2).

In slices exposed to SiO_2 and PS-COOH nanoparticles no effects on viability were observed at any concentration and in all of the organs tested. In contrast, exposure to PS-NH₂ nanoparticles led to a significant loss of viability in all the organs, with stronger effects on kidney and lung slices (Figure 1). In line with the viability results, hematoxylin and eosin staining of liver, lung, and kidney slices exposed to PS-NH₂ nanoparticles showed severe morphological damage (Figure 2). Dead areas (necrotic and/or apoptotic) characterized by nuclear dissolution and condensation were observed in all tissue slices, but important differences could be detected in the different organs (as discussed in more detail later).

As a next step, to compare nanoparticle uptake and distribution in the different organs, tissue slices were exposed to a series of fluorescently labeled nanoparticles (Figures 3–5), including 50 nm SiO_2 , 40 nm and 200 nm PS-COOH. Confocal imaging of

transversal sections showed that in liver, kidney, and lung slices uptake was present for all nanoparticles tested. However, uptake levels were minimal in the kidneys and very high in the lungs. Additionally, immunostaining by CD68 indicated that, as observed *in vivo*, in all organs the macrophages internalized a higher amount of nanoparticles.

Given the high accumulation of nanoparticles in the lungs, especially in the case of the smaller 40 nm PS-COOH, we then performed additional studies by flow cytometry to confirm the imaging results and determine in a more quantitative way nanoparticle uptake kinetics in the macrophages and all other cells over time after enzymatic digestion of the tissue (see Materials and Methods for details and Supplementary Figure S6 for gating strategy). The results are compared to those previously obtained in liver slices with the same nanoparticles (Bartucci et al. 2020).

Flow cytometry analysis showed that both uptake levels and the fraction of cells taking up nanoparticles increased over time (Figure 6(a)). Already after only 1 h almost 40% of the macrophages in the lungs slices accumulated nanoparticles (Figure 6(b)), as opposed to only around 10% for the Kupffer cells in the liver. At 48 h almost 80% of the macrophages contained nanoparticles.

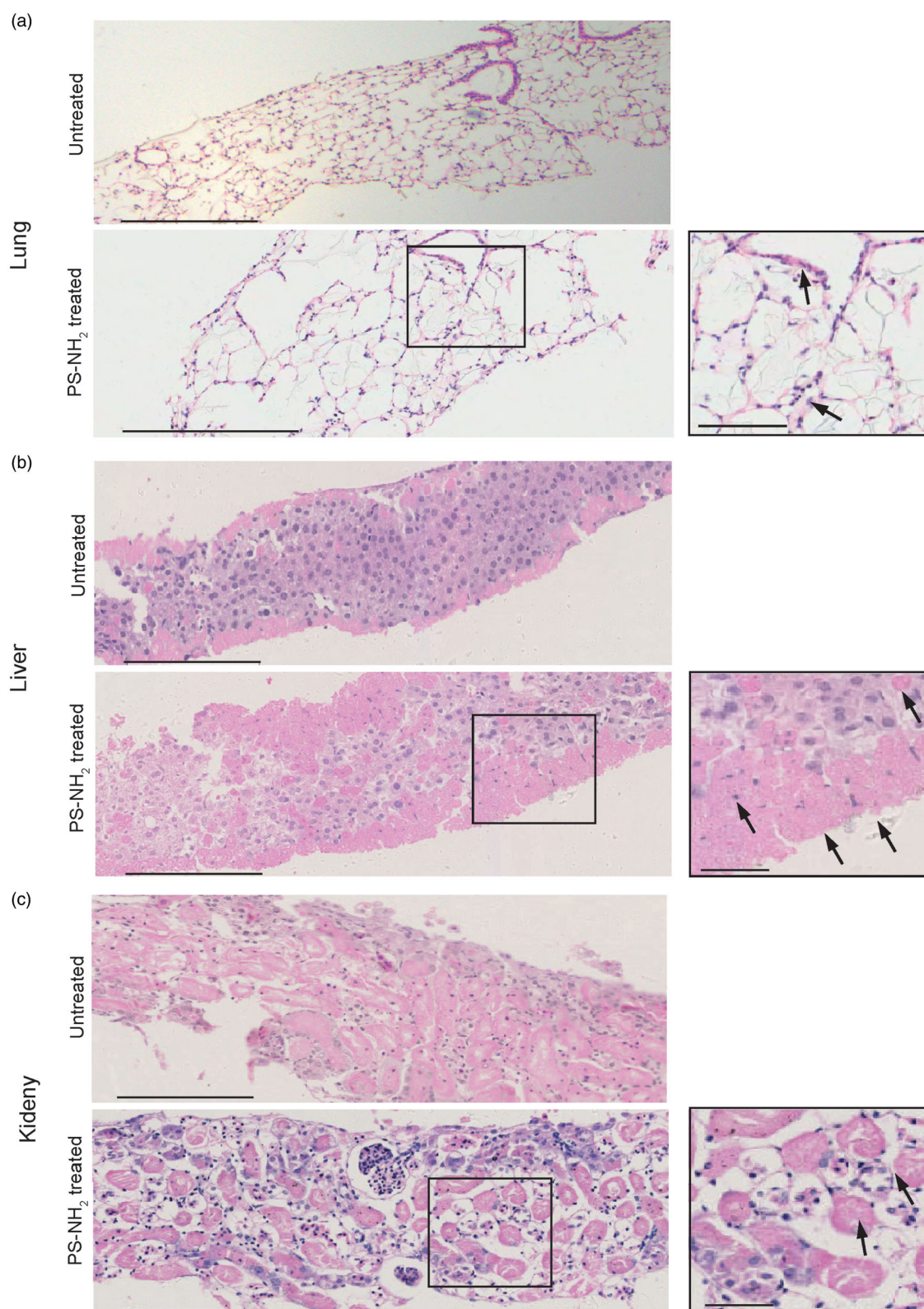


Figure 2. Morphological assessment of murine lung, liver, and kidney slices exposed to PS-NH₂ nanoparticles. Tissue morphology after 48 h of lung (a), liver (b), and kidney (c) untreated slices and slices exposed to 50 µg/mL PS-NH₂. Cross sections of tissue slices were imaged after hematoxylin and eosin staining. Scale bar: 200 µm for left side images and 50 µm for zoomed details on the right. Exposure to PS-NH₂ led to decreased viability in all organs and severely damaged morphology. In the lung slices exposed to the nanoparticles (a), severe damage to the alveoli was visible, together with apoptotic bodies (shown by the arrows). In the liver (b), tissue damage was visible mainly in the outer cell layers, including anucleated cells, apoptotic bodies, and apoptotic cell debris (as indicated for some examples by the arrows). In the kidneys (c), severe damage was visible throughout all tissue section with severe nuclear dissolution especially on proximal tubuli and necrotic tissue (see arrows for some examples).

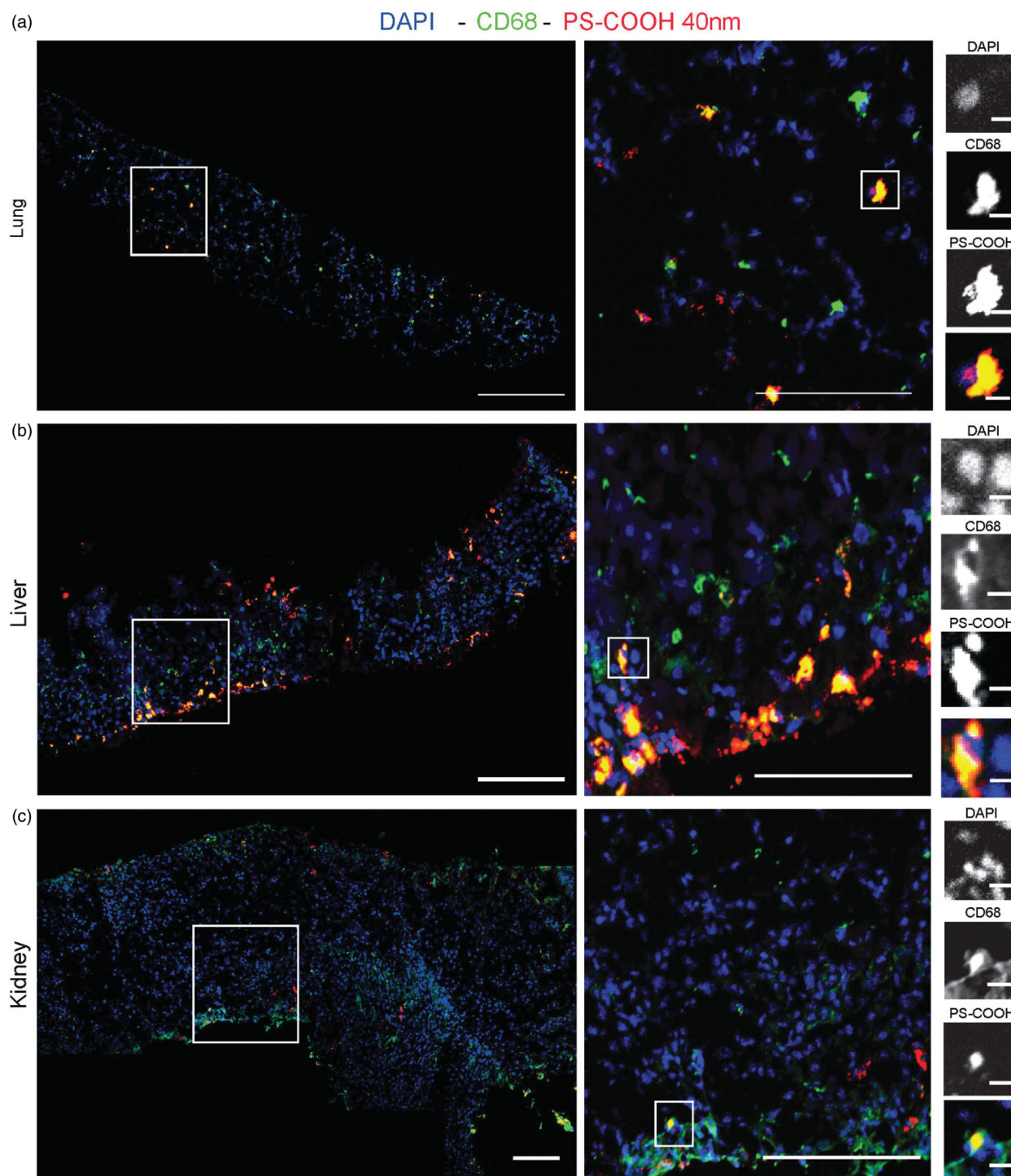


Figure 3. Confocal fluorescence images of murine lung (a), liver (b), and kidney (c) slices exposed to 40 nm PS-COOH nanoparticles. Cross-sections were acquired by confocal fluorescence microscopy after exposure for 48 h to $10 \mu\text{g/mL}$ 40 nm dark-red PS-COOH nanoparticles in medium supplemented with 5% FBS. The indicated areas are shown at increased magnification to the right. For a and c, scale bars, from left: 200, 100, and $10 \mu\text{m}$. For b, scale bars from left: 200 and $100 \mu\text{m}$. Blue: DAPI-stained nuclei. Red: nanoparticles. Green: CD68-labeled macrophages (For interpretation of the references to colours in this legend, please refer to the web version of this article.). In the lungs (a), despite the presence of agarose, high nanoparticle uptake into the tissue was observed, and preferential accumulation by macrophages. In the liver (b), nanoparticle uptake into the tissue was clearly visible, as well as high uptake by macrophages, especially at the border of the tissue slices. (b). In the kidneys (c), uptake levels were lower and limited to the first cell layers.

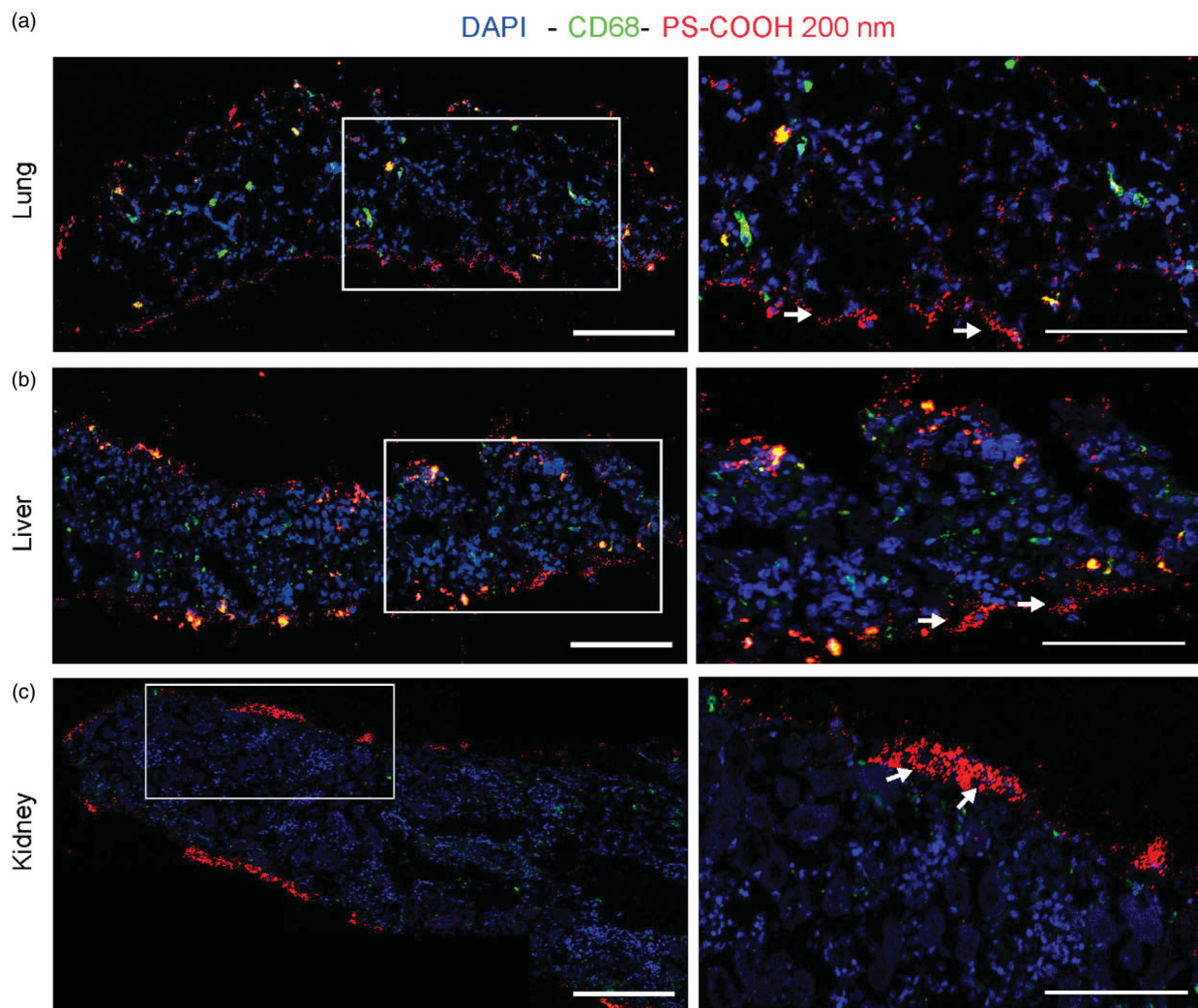


Figure 4. Confocal fluorescence images of murine lung (a), liver (b), and kidney (c) slices exposed to 200 nm PS-COOH nanoparticles. Cross-sections were acquired by confocal fluorescence microscopy after exposure for 48 h to 10 $\mu\text{g/mL}$ 200 nm orange PS-COOH nanoparticles in medium supplemented with 5% FBS. The indicated areas are shown at increased magnification to the right. For a, b and c, scale bars, from left: 200 and 100 μm . Blue: DAPI-stained nuclei. Red: nanoparticles. Green: CD68-labeled macrophages (For interpretation of the references to colours in this legend, please refer to the web version of this article.). In the lungs (a) and the liver (b), uptake in the macrophages was observed, but also in other cells (as indicated by the arrows). In the kidneys (c), lower nanoparticle uptake and less penetration into the tissue were observed, as well as strong nanoparticle adsorption on the edge of the slices, as indicated by the arrows.

Furthermore, at all times, the macrophages were the cells with the higher cell fluorescence intensity (Figure 6(c)), especially evident at the earlier exposure times (1 and 3 h).

As a final step, given the higher uptake levels observed in the lung and liver slices (Figures 3–6), and preferential accumulation in the macrophages, we investigated whether potential inflammatory responses and effects on macrophage polarization could be detected in these organs after nanoparticle exposure. This was done by measuring the expression levels of a panel of pro- and anti-inflammatory cytokines (Dinarelli 1997; Figure 6; IL-1 β , IL-

6, and IL-10), together with *ym1* (chitinase-like 3) and *MHCII* (major histocompatibility complex class II) as markers for M1 and M2 macrophage differentiation (Italiani and Boraschi 2014), respectively (Figure 7). The results showed that no significant changes in expression levels were observed for the selected panel of markers.

Discussion

Appropriate models are required to study *in vitro* potential effects induced by nanomaterials in the organs where they accumulate following exposure.

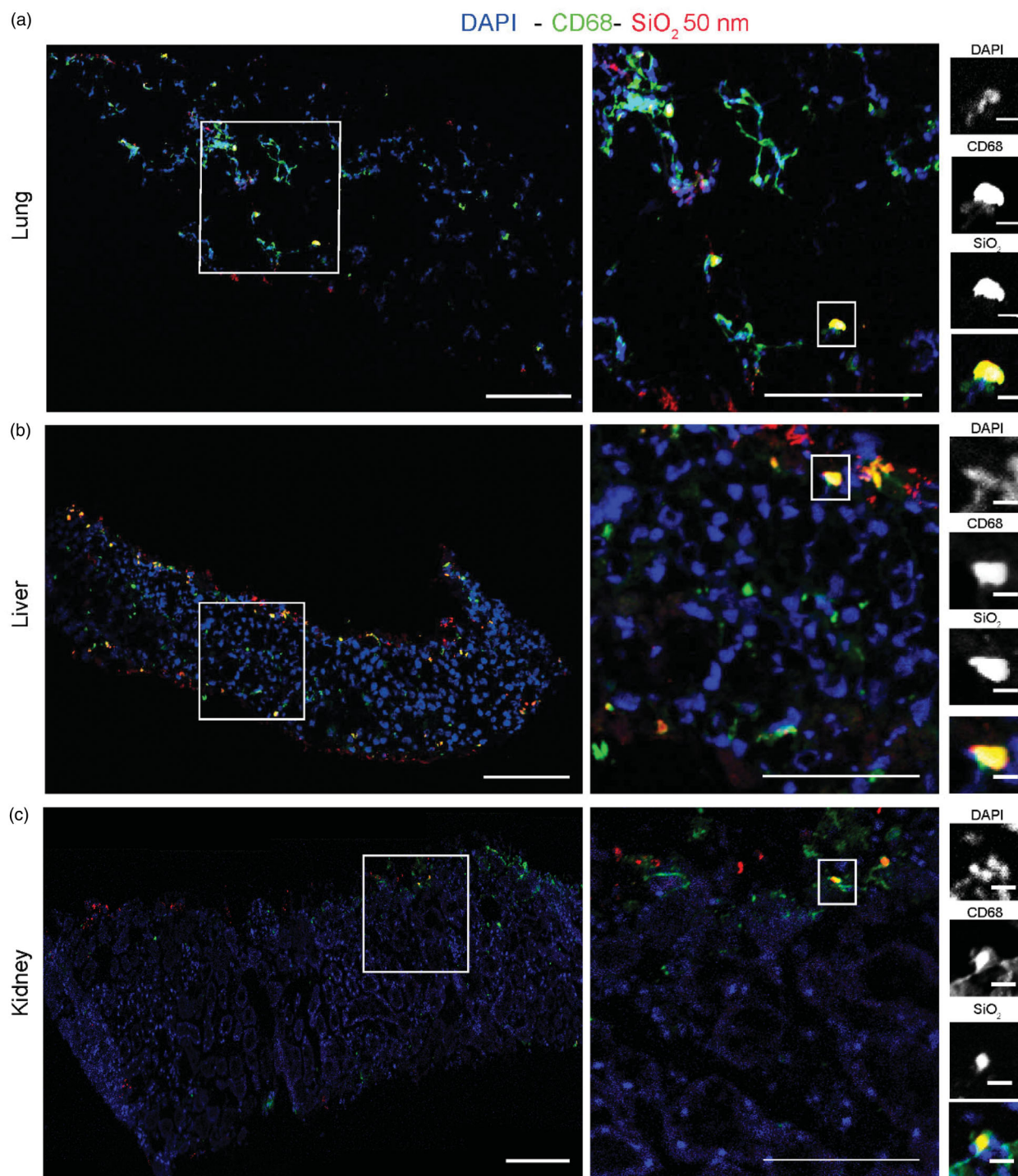


Figure 5. Confocal fluorescence images of murine lung (a), liver (b), and kidney (c) slices exposed to 50 nm SiO_2 nanoparticles. Cross-sections were acquired by confocal fluorescence microscopy after exposure for 48 h to 25 $\mu\text{g}/\text{mL}$ 50 nm red SiO_2 nanoparticles in medium supplemented with 5% FBS. The indicated areas are shown at increased magnification to the right. For a and b, scale bars, from left: 200, 100, and 10 μm . For c, scale bars: 200 and 100 μm . Blue: DAPI-stained nuclei. Red: nanoparticles. Green: CD68-labeled macrophages (For interpretation of the references to colours in this legend, please refer to the web version of this article.). In slices exposed to SiO_2 nanoparticles the results were comparable to what observed for the 40 nm PS-COOH, including higher uptake by the macrophages, however, uptake levels seemed overall lower, most probably due to the lower fluorescence intensity of these nanoparticles.

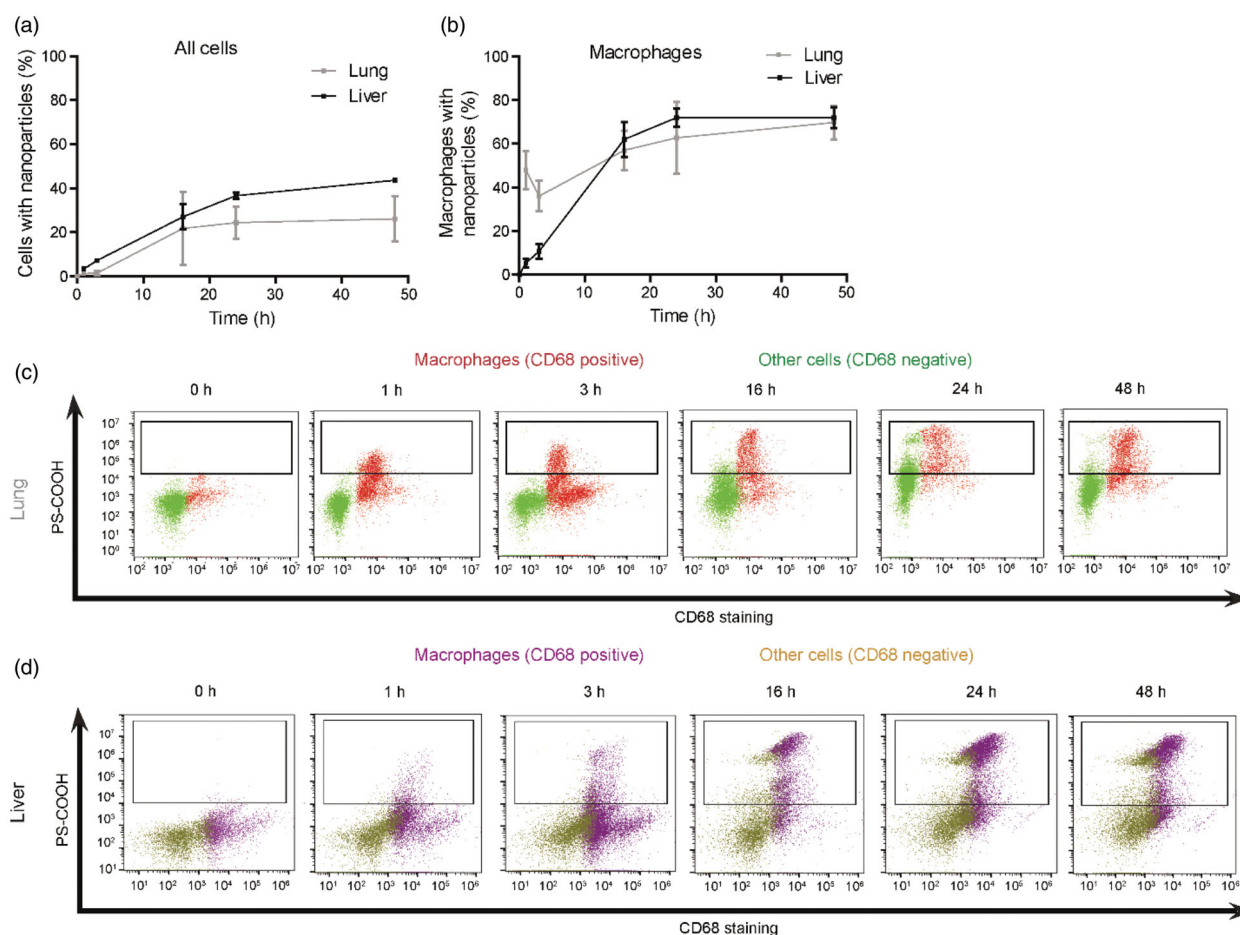


Figure 6. Flow cytometry analysis of nanoparticle uptake by primary macrophages and all other cells recovered from murine lung and liver slices exposed to PS-COOH 40 nm nanoparticles over time. Lung slices were exposed to 25 $\mu\text{g/mL}$ 40 nm dark-red PS-COOH nanoparticles in medium supplemented with 5% FBS for up to 48 h. Then cells were recovered from the tissue as described in the Materials and Methods and their fluorescence intensity measured by flow cytometry. The results obtained in liver slices exposed to the same nanoparticles in the same conditions are reproduced from previously published work (Bartucci et al. 2020) to allow direct comparison of uptake kinetics and distribution in the two organs. a: fraction of cells with nanoparticles; b: fraction of macrophages with nanoparticles. The average and standard deviation of the results obtained in three independent experiments are shown (with the exception of the 16 h sample in lung slices, which was performed only in two experiments). For each condition 25 000–50 000 individual cells were acquired in the case of lung slices (20 000–70 000 for liver tissue). c,d: Representative double scatter plots of cell fluorescence intensity in the nanoparticle channel (nanoparticle uptake, PS-COOH) versus CD68 staining in the lungs (c) and in the liver (d). The macrophages (CD68-positive cells) and all other cells (CD68-negative) are shown in different colors (please refer to the web version of this article). The results show that in both organs uptake increased over time in both macrophages and all other cells with nanoparticles, but at all times the average intensity of macrophages with nanoparticles was higher than that of all other cells with nanoparticles. However, in the lungs uptake kinetics in the macrophages were faster than in the liver Kupffer cells and already after only 1 h of exposure around 40% of the macrophages had internalized nanoparticles, as opposed to only around 10% in the case of the Kupffer cells.

While simple cell cultures are for sure advantageous for a first screening of potential effects induced by nanoparticles on cells, more advanced *in vitro* models, better resembling the complexity of the *in vivo* environment and specific features of the different organs in which nanoparticles distribute, ideally could help to gain information on potential nanoparticle outcomes *in vivo*.

Here, we have used murine tissue slices as a 3D *ex vivo* model to perform for the first time a comparative study of nanoparticle impact, uptake, and distribution in three of the major organs in which they distribute *in vivo*, namely liver, kidneys, and lungs. By using a panel of well-characterized nanoparticles, we combined multiple essays, including viability studies, morphological analysis, and

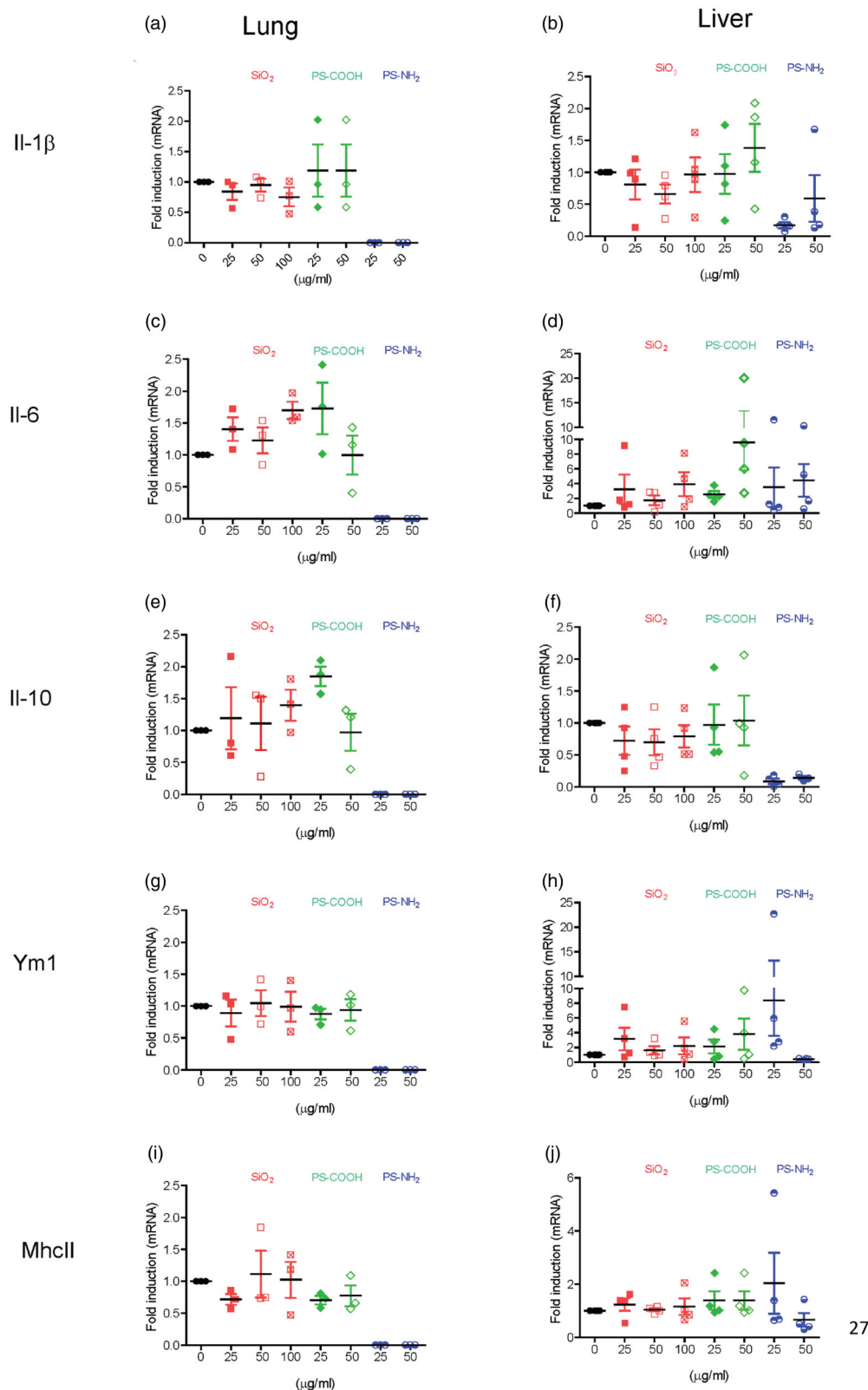


Figure 7. mRNA expression levels of *IL-1 β* , *IL-6*, *IL-10*, *Ym1*, and *MHCII* in murine lung and liver slices exposed to nanoparticles. qRT-PCR analysis of inflammatory cytokines and polarization markers in lung and liver slices exposed to 25, 50, and 100 $\mu\text{g/ml}$ 50 nm SiO_2 , 25 and 50 $\mu\text{g/ml}$ PS-COOH and PS-NH₂ nanoparticles for 48 h. Results are shown as fold change over the results obtained in untreated control slices, calculated as described in the Materials and Methods. The data are the average of three or four independent experiments and the error bars represent the standard error of the mean (SEM). Each symbol represents an independent experiment. Kruskal–Wallis statistic followed by Dunnett’s multiple comparisons test was performed on ΔCt values.

nanoparticle uptake and distribution by microscopy to compare the outcomes in the different organs.

Prior to exposure to tissue, the dispersions in medium with serum were characterized both as soon as prepared and after 24 h of incubation in the conditions applied for exposure to tissue. Even though for slice maintenance serum-free medium is usually applied, nanoparticle exposure was always performed in medium supplemented with 5% FBS to allow corona formation on the nanoparticles (Monopoli et al. 2012). Low concentrations of bovine serum were used here as a first approximation to avoid unrealistic exposure to bare surfaces, which could elicit strong toxic responses (Lesniak et al. 2012; Duan et al. 2015). Given the impact of the corona on nanoparticle outcomes at cell level, it will be important for future studies to use biological fluids relevant to the different exposure scenarios and tissue studied, such as the use of murine serum proteins on murine tissue, as well as lung surfactant proteins for studies with lung slices. The results showed that the SiO₂ and PS-COOH nanoparticles formed homogenous dispersions in medium with serum, which remained stable also after 24 h in the conditions applied for tissue studies. On the contrary, the PS-NH₂ polystyrene showed agglomeration once dispersed in medium with serum.

We then compared the effects of nanoparticle exposure on tissue viability for the different organs (Figure 1). The ATP concentration normalized by protein content was used as an indicator of slice viability. Initial tests showed that exposure to 100 µg/mL PS-NH₂ was very toxic to liver slices (Supplementary Figure S2): in these conditions, ATP was not detectable, indicating death of the tissue. For this reason, additional studies were performed by exposing tissue slices to up to 50 µg mL⁻¹ PS-COOH and PS-NH₂ nanoparticles, while for SiO₂ nanoparticles higher concentrations were used (50, 100 and 200 µg/mL), also to take into account the different density of the two materials and expose slices to comparable numbers of nanoparticles. Interestingly, comparison with previous data (Bartucci et al. 2020) obtained exposing liver slices from rat and human tissue to 100 µg/mL of the same PS-NH₂ in the same conditions (Supplementary Figure S2) showed that despite the same size and mass of the liver slices, these nanoparticles were more toxic in mouse and human

liver. Thus, tissue slices can also be used to gain information on important species differences in responses to nanoparticles, including in humans.

In slices exposed to SiO₂ and PS-COOH nanoparticles no effects on viability were observed at any concentration and in all of the organs tested. In contrast, as reported in several *in vitro* studies (Bexiga et al. 2011; Wang et al. 2013) and in agreement with our previous findings on liver slices (Bartucci et al. 2020), exposure to PS-NH₂ nanoparticles led to a significant loss of viability in all the organs (Figure 1). Liver slices seemed to be slightly more resistant than kidney and lung slices. However, a direct comparison among the organs is difficult, considering the different masses of tissue and – in the case of lung slices – the additional presence of agarose.

In line with the viability results, hematoxylin and eosin staining of liver, lung, and kidney slices exposed to PS-NH₂ nanoparticles (Figure 2) showed severe morphological damage, with interesting differences in the different organs. More in detail, in the lungs, because of their open structure, a much higher number of cells are in direct contact with the nanoparticles, and as a result of this, the damage was very severe. Thus, after 48 h exposure, cleaved alveoli, pyknotic nuclei, and apoptotic bodies were visible practically everywhere in the treated lung slices, together with necrotic areas (Figure 2(a)). Correspondingly almost no ATP could be detected (Figure 1 and corresponding Supplementary Figure S3). In previous work on liver slices, we studied more in detail the mechanism of toxicity in response to the same PS-NH₂ nanoparticles and we showed activation of apoptosis (Bartucci et al. 2020). The presence of apoptotic bodies in the lungs may suggest that similar mechanisms may be present also in this tissue.

In liver and kidney, because of their more compact and closed structure, we may expect that a lower number of cells are initially in contact with the tissue. Nevertheless, exposure to the PS-NH₂ had strong effects on tissue viability and morphology in both organs, but, interestingly, the toxic effects in the kidney were stronger than in the liver (Figures 1 and 2(b,c)). More in detail, in the liver (Figure 2(b)), morphological analysis showed that tissue damage was evident in the outer cell layers, where hematoxylin staining was lower in

comparison to healthy tissue, as a consequence of the toxicity induced by the PS-NH₂ nanoparticles. In these outer layers, anucleated cells and apoptotic bodies were also visible (as shown by the arrows in Figure 2(b)), in agreement with previous results in liver slices, which showed activation of apoptosis (Bartucci et al. 2020). On the contrary, in the kidney (Figure 2(c)), severe damage was visible throughout the full thickness of the section, including loss of the morphological structure of glomeruli and severe effects on the proximal tubuli. Anucleated cells and pyknotic nuclei were clearly visible (also indicated by arrows), suggesting severe necrotic damage, without clear apoptotic features. It is important to mention that in kidneys and lungs, tissue damage was visible after 48 h culture also in the untreated slices, but the effects described were clearly stronger in the slices exposed to the PS-NH₂ nanoparticles.

We then used a panel of fluorescently labeled nanoparticles to compare uptake levels and distribution in the different organs. In order not to confuse uptake and distribution outcomes with effects due to toxicity, this study was performed using the 50 nm SiO₂ nanoparticles and 40 nm PS-COOH, for which no toxicity was observed (Figure 1). Additionally, 200 nm PS-COOH were also included to determine eventual differences for bigger nanoparticles. Confocal microscopy was used to obtain images of entire transversal sections of the tissue slices from the 3 organs after exposure to the 3 different nanoparticles. In all cases uptake was present, but, also in relation to uptake, interesting differences were observed in the different organs.

For the 40 nm PS-COOH (Figure 3), in lung slices a remarkable uptake and accumulation of nanoparticles was observed. This was surprising also considering the presence of agarose, which is used to prevent collapse of the tissue structure, and which might have compromised nanoparticle studies on lung slices. In contrast, in the liver, most of the nanoparticles were observed in the first cell layers, and only few were reaching deeper cells in the slice. In kidney slices, uptake levels were clearly lower than in the other organs, even for the cells of the outer layers. This may be a consequence of the very tight and compact morphological structure of the kidneys. Similarly, penetration of nanoparticles into deeper cell layers within the tissue was also

very limited. Interestingly, immunostaining with CD68 indicated that in all organs the macrophages preferentially internalized a higher number of nanoparticles, the effect being more evident in liver and lungs, because of the higher uptake. The same phenomenon was observed also in rat liver slices, where we also demonstrated migration of the macrophages at the slice borders toward the site of nanoparticle exposure (Bartucci et al. 2020). Here, the effect was particularly clear in the lungs, where accumulation of nanoparticles was visible almost exclusively in macrophages rather than in other cells, despite the open lung morphology, which allows almost all cells to be in direct contact with the nanoparticles.

In the case of the 200 nm PS-COOH nanoparticles (Figure 4), in the lungs, more nanoparticles were stuck on the edge of the slices and accumulation in macrophages as well as in other cells was observed (as shown by the white arrows in Figure 4(a)). In the liver (Figure 4(b)), uptake was clearly visible, but as expected because of the larger size, in the second and third cell layers it was lower in comparison to what observed with the smaller nanoparticles. Moreover, smaller differences were observed between the uptake by macrophages and all other cells. Uptake was even lower in the kidneys, with many nanoparticles adsorbed at the edge of the slices.

Finally, for the 50 nm SiO₂ (Figure 5), the results were comparable to what observed for the 40 nm PS-COOH, but because of their lower fluorescence, uptake was more difficult to visualize.

It is interesting to note that while the fluorescence distribution studies showed that in the kidneys and liver uptake was limited to the outer cell layers, toxicity in kidney slices exposed to the PS-NH₂ nanoparticles was clearly visible throughout all tissue (Figure 2(c)). It is likely that the outer cell layers are those first in contact with nanoparticles, however as these outer cells die upon exposure to the toxic nanoparticles and the tissue structure is compromised, also the inner layers of cells may get in direct contact with the nanoparticles. This can explain the damage observed throughout all thickness of the kidney sections (Figure 2(c)). In contrast, in the case of the liver, the damage remained confined to the outer cell layers (Figure 2(b)) and in

agreement with this, the loss of viability was not as severe as in the case of the kidneys (Figure 1).

After the comparative uptake and distribution study with the panel of nanoparticles in the three organs, we performed additional studies to gain further insights on nanoparticle uptake kinetics in the tissue. This additional study was done for the case of lung slices exposed to the 40 nm PS-COOH, for which high uptake was observed (Figure 2(b)). Thus, we used enzymatic digestion of the tissue to recover individual cells and quantify uptake kinetics by flow cytometry (Figure 6). We include for comparison similar data previously obtained in murine liver slices with the same nanoparticles (Bartucci et al. 2020), to determine eventual differences in uptake kinetics and distribution in the lungs and the liver.

The results showed that in both organs, the fraction of cells taking up nanoparticles increased over time. Furthermore, at all times, the macrophages were the cells with the higher cell fluorescence intensity, confirming their higher nanoparticle uptake. However, in the liver slices (Bartucci et al. 2020), in the first hours of exposure only around 10% of the Kupffer cells (resident liver macrophages) accumulated nanoparticles, as opposed to 40–60% of the macrophages in the lungs. Additionally, in the lung slices, higher accumulation in macrophages was already visible after only 1 h, suggesting that uptake kinetics were faster. This is the first time that nanoparticle uptake kinetics are obtained in lung tissue and compared for macrophages and all other cells. It would be interesting in the future to perform similar studies to compare uptake in the other different cell types present in the lungs, and also using nanoparticles of different sizes and materials.

As a final step, having observed higher uptake in lung and liver slices and preferential accumulation in the macrophages, we performed additional studies in these organs to determine whether nanoparticle exposure induced inflammatory responses and effects on macrophage polarization. To this aim, we quantified the expression levels of a panel of pro- and anti-inflammatory cytokines (Dinarelli 1997; Figure 6; IL-1 β , IL-6, and IL-10), together with ym1 (chitinase-like 3) and MHCII (major histocompatibility complex class II) as markers for M1 and M2 macrophage differentiation (Italiani and Boraschi

2014), respectively (Figure 7). From lung slices exposed to PS-NH₂ nanoparticles, low concentrations of mRNA were extracted, most probably due to the strong toxic effects of the nanoparticles at both concentrations tested. In all other conditions and both in liver and kidney slices, no significant changes in expression levels were observed, suggesting that in these conditions these nanoparticles induced strong cell death without effects at gene expression level on macrophage polarization or inflammatory responses. It would be interesting in future to test whether changes in these markers may be visible at shorter exposure times, when the damage to tissue is lower and responses to the nanoparticles may be detected more easily.

In conclusion, in this work we show that tissue slices from different organs can be used as a 3D *ex vivo* model to directly compare nanoparticle uptake, distribution, and impact in the different organs in which they distribute. Different nanoparticles can be tested at different concentrations and exposure times in slices from multiple organs, all using only one animal at a time. By comparing nanoparticle outcomes in different tissues under the same conditions, important differences in uptake efficiency and distribution, as well as in the responses to nanoparticles at organ level can be obtained. This makes this model a rather unique addition to the available tools for nanosafety assessment.

Acknowledgments

The authors thank M. J. R. Ruigrok for technical help for lung extraction and preparation, and A. van der Meer for technical help for the collection of ATP data. Confocal microscopy was performed at the UMCG Imaging and Microscopy Center (UMIC).

Disclosure statement

The authors report no conflict of interest.

Funding

A.S. and Y.L.B. kindly acknowledge the University of Groningen for funding (Rosalind Franklin Fellowship). Additional funding to A.S. from the European Research Council (ERC) under the European Union's Horizon 2020 research and innovation program [grant agreement no. 637614 (NanoPaths)] is also acknowledged.

Data availability statement

The data that support the findings of this study are available from the corresponding author A.S. upon reasonable request.

References

- Ahlberg, S., A. Antonopulos, J. Diendorf, R. Dringen, M. Eppele, R. Flöck, W. Goedecke, et al. 2014. "PVP-Coated, Negatively Charged Silver Nanoparticles: A Multi-Center Study of Their Physicochemical Characteristics, Cell Culture and in Vivo Experiments." *Beilstein Journal of Nanotechnology* 5: 1944–1965. doi:10.3762/bjnano.5.205.
- Armstead, A. L., and B. Li. 2016. "Nanotoxicity: Emerging Concerns Regarding Nanomaterial Safety and Occupational Hard Metal (WC-Co) Nanoparticle Exposure." *International Journal of Nanomedicine* 11: 6421–6433. doi:10.2147/IJN.S121238.
- Barnes, C. A., A. Elsaesser, J. Arkusz, A. Smok, J. Palus, A. Leśniak, A. Salvati, et al. 2008. "Reproducible Comet Assay of Amorphous Silica Nanoparticles Detects No Genotoxicity." *Nano Letters* 8 (9): 3069–3074. doi:10.1021/nl801661w.
- Bartneck, M., K. T. Warzecha, and F. Tacke. 2014. "Therapeutic Targeting of Liver Inflammation and Fibrosis by Nanomedicine." *Hepatobiliary Surgery and Nutrition* 3 (6): 364–376. doi:10.3978/j.issn.2304-3881.2014.11.02.
- Bartucci, R., C. Åberg, B. N. Melgert, Y. L. Boersma, P. Olinga, and A. Salvati. 2020. "Time-Resolved Quantification of Nanoparticle Uptake, Distribution, and Impact in Precision-Cut Liver Slices." *Small* : 1906523. doi:10.1002/sml.201906523.
- Bexiga, M. G., J. A. Varela, F. Wang, F. Fenaroli, A. Salvati, I. Lynch, J. C. Simpson, and K. A. Dawson. 2011. "Cationic Nanoparticles Induce Caspase 3-, 7- and 9-Mediated Cytotoxicity in a Human Astrocytoma Cell Line." *Nanotoxicology* 5 (4): 557–567. doi:10.3109/17435390.2010.539713.
- Bierkandt, F. S., L. Leibrock, S. Wagener, P. Laux, and A. Luch. 2018. "The Impact of Nanomaterial Characteristics on Inhalation Toxicity." *Toxicology Research* 7 (3): 321–346. doi:10.1039/c7tx00242d.
- Burden, N., K. Aschberger, Q. Chaudhry, M. J. D. Clift, S. H. Doak, P. Fowler, H. Johnston, R. Landsiedel, J. Rowland, and V. Stone. 2017. "The 3Rs as a Framework to Support a 21st Century Approach for Nanosafety Assessment." *Nano Today* 12: 10–13. doi:10.1016/j.nantod.2016.06.007.
- Choi, C. H. J., J. E. Zuckerman, P. Webster, and M. E. Davis. 2011. "Targeting Kidney Mesangium by Nanoparticles of Defined Size." *Proceedings of the National Academy of Sciences* 108 (16): 6656–6661. doi:10.1073/pnas.1103573108.
- Choi, H. S., Y. Ashitate, J. H. Lee, S. H. Kim, A. Matsui, N. Insin, M. G. Bawendi, M. Semmler-Behnke, J. V. Frangioni, and A. Tsuda. 2010. "Rapid Translocation of Nanoparticles from the Lung Airspaces to the Body." *Nature Biotechnology* 28 (12): 1300–1303. doi:10.1038/nbt.1696.
- de Graaf, I. A. M., P. Olinga, M. H. de Jager, M. T. Merema, R. de Kanter, E. G. van de Kerkhof, and G. M. M. Groothuis. 2010. "Preparation and Incubation of Precision-Cut Liver and Intestinal Slices for Application in Drug Metabolism and Toxicity Studies." *Nature Protocols* 5 (9): 1540–1551. doi:10.1038/nprot.2010.111.
- De Jong, W. H., W. I. Hagens, P. Krystek, M. C. Burger, A. J. A. M. Sips, and R. E. Geertsma. 2008. "Particle Size-Dependent Organ Distribution of Gold Nanoparticles after Intravenous Administration." *Biomaterials* 29 (12): 1912–1919. doi:10.1016/j.biomaterials.2007.12.037.
- Dinareello, C. A. 1997. "Role of Pro- and anti-Inflammatory Cytokines During Inflammation: experimental and Clinical Findings." *Journal of Biological Regulators and Homeostatic Agents* 11 (3): 91–103.
- Du, B., M. Yu, and J. Zheng. 2018. "Transport and Interactions of Nanoparticles in the Kidneys." *Nature Reviews Materials* 3 (10): 358–374. doi:10.1038/s41578-018-0038-3.
- Duan, G., S. Kang, X. Tian, J. A. Garate, L. Zhao, C. Ge, and R. Zhou. 2015. "Protein Corona Mitigates the Cytotoxicity of Graphene Oxide by Reducing Its Physical Interaction with Cell Membrane." *Nanoscale* 7 (37): 15214–15224. doi:10.1039/c5nr01839k.
- Fadeel, B., L. Farcas, B. Hardy, S. Vázquez-Campos, D. Hristozov, A. Marcomini, I. Lynch, E. Valsami-Jones, H. Alenius, and K. Savolainen. 2018. "Advanced Tools for the Safety Assessment of Nanomaterials." *Nature Nanotechnology* 13 (7): 537–543. doi:10.1038/s41565-018-0185-0.
- Haute, D. V., and J. M. Berlin. 2017. "Challenges in Realizing Selectivity for Nanoparticle Biodistribution and Clearance: lessons from Gold Nanoparticles." *Therapeutic Delivery* 8 (9): 763–774. doi:10.4155/tde-2017-0057.
- Huh, D., G. A. Hamilton, and D. E. Ingber. 2011. "From 3D Cell Culture to Organs-on-Chips." *Trends in Cell Biology* 21 (12): 745–754. doi:10.1016/j.tcb.2011.09.005.
- Italiani, P., and D. Boraschi. 2014. "From Monocytes to M1/M2 Macrophages: Phenotypical vs. Functional Differentiation." *Frontiers in Immunology* 5: 514. doi:10.3389/fimmu.2014.00514.
- Kim, I.-Y., E. Joachim, H. Choi, and K. Kim. 2015. "Toxicity of Silica Nanoparticles Depends on Size, Dose, and Cell Type." *Nanomedicine : Nanotechnology, Biology, and Medicine* 11 (6): 1407–1416. doi:10.1016/j.nano.2015.03.004.
- Klein, S. G., T. Serchi, L. Hoffmann, B. Blömeke, and A. C. Gutleb. 2013. "An Improved 3D Tetraculture System Mimicking the Cellular Organisation at the Alveolar Barrier to Study the Potential Toxic Effects of Particles on the Lung." *Particle and Fibre Toxicology* 10 (1): 31. doi:10.1186/1743-8977-10-31.
- Kreyling, W. G., M. Semmler-Behnke, S. Takenaka, and W. Möller. 2013. "Differences in the Biokinetics of Inhaled

- Nano- Versus Micrometer-Sized Particles." *Accounts of Chemical Research* 46 (3): 714–722. doi:10.1021/ar300043r.
- Krug, H. F. 2014. "Nanosafety Research-Are We on the Right Track?" *Angewandte Chemie International Edition* 53 (46): 12304–12319. doi:10.1002/anie.201403367.
- Kusaka, T., M. Nakayama, K. Nakamura, M. Ishimiya, E. Furusawa, and K. Ogasawara. 2014. "Effect of Silica Particle Size on Macrophage Inflammatory Responses." *PLoS One* 9 (3): e92634. doi:10.1371/journal.pone.0092634.
- Lesniak, A., F. Fenaroli, M. P. Monopoli, C. Åberg, K. A. Dawson, and A. Salvati. 2012. "Effects of the Presence or Absence of a Protein Corona on Silica Nanoparticle Uptake and Impact on Cells." *ACS Nano* 6 (7): 5845–5857. doi:10.1021/nn300223w.
- Liu, J., M. Yu, C. Zhou, and J. Zheng. 2013. "Renal Clearable Inorganic Nanoparticles: A New Frontier of Bionanotechnology." *Materials Today* 16 (12): 477–486. doi:10.1016/j.mattod.2013.11.003.
- Longmire, M., P. L. Choyke, and H. Kobayashi. 2008. "Clearance Properties of Nano-Sized Particles and Molecules as Imaging Agents: Considerations and Caveats." *Nanomedicine (London, England)* 3 (5): 703–717. doi:10.2217/17435889.3.5.703.
- Loos, C., T. Syrovets, A. Musyanovych, V. Mailänder, K. Landfester, G. U. Nienhaus, and T. Simmet. 2014. "Functionalized Polystyrene Nanoparticles as a Platform for Studying Bio-nano interactions." *Beilstein Journal of Nanotechnology* 5: 2403–2412. doi:10.3762/bjnano.5.250.
- Mahto, S. K., V. Charwat, P. Ertl, B. Rothen-Rutishauser, S. W. Rhee, and J. Sznitman. 2015. "Microfluidic Platforms for Advanced Risk Assessments of Nanomaterials." *Nanotoxicology* 9 (3): 381–395. doi:10.3109/17435390.2014.940402.
- Monopoli, M. P., C. Åberg, A. Salvati, and K. A. Dawson. 2012. "Biomolecular Coronas Provide the Biological Identity of Nanosized Materials." *Nature Nanotechnology* 7 (12): 779–786. doi:10.1038/nnano.2012.207.
- Nel, A., T. Xia, L. Mädler, and N. Li. 2006. "Toxic Potential of Materials at the Nanolevel." *Science (New York, N.Y.)* 311 (5761): 622–627. doi:10.1126/science.1114397.
- Neuhaus, V., O. Danov, S. Konzok, H. Obernolte, S. Dehmel, P. Braubach, D. Jonigk, et al. 2018. "Assessment of the Cytotoxic and Immunomodulatory Effects of Substances in Human Precision-Cut Lung Slices." *Journal of Visualized Experiments* (135): 57042. doi:10.3791/57042.
- Oberdörster, G., E. Oberdörster, and J. Oberdörster. 2005. "Nanotoxicology: An Emerging Discipline Evolving from Studies of Ultrafine Particles." *Environmental Health Perspectives* 113 (7): 823–839. doi:10.1289/ehp.7339.
- Olinga, P., and D. Schuppan. 2013. "Precision-Cut Liver Slices: A Tool to Model the Liver Ex Vivo." *Journal of Hepatology* 58 (6): 1252–1253. doi:10.1016/j.jhep.2013.01.009.
- Osman, G., J. Rodriguez, S. Y. Chan, J. Chisholm, G. Duncan, N. Kim, A. L. Tatler, et al. 2018. "PEGylated Enhanced Cell Penetrating Peptide Nanoparticles for Lung Gene Therapy." *Journal of Controlled Release : Official Journal of the Controlled Release Society* 285: 35–45. doi:10.1016/j.jconrel.2018.07.001.
- Paranjpe, M., V. Neuhaus, J. H. Finke, C. Richter, T. Gothsch, A. Kwade, S. Büttgenbach, A. Braun, and C. C. Müller-Goymann. 2013. "In Vitro and Ex Vivo Toxicological Testing of Sildenafil-Loaded Solid Lipid Nanoparticles." *Inhalation Toxicology* 25 (9): 536–543. doi:10.3109/08958378.2013.810315.
- Park, E.-J., J. Roh, Y. Kim, and K. Choi. 2011. "A Single Instillation of Amorphous Silica Nanoparticles Induced Inflammatory Responses and Tissue Damage Until Day 28 after Exposure." *Journal of Health Science* 57 (1): 60–71. doi:10.1248/jhs.57.60.
- Park, J.-K., T. Utsumi, Y.-E. Seo, Y. Deng, A. Satoh, W. M. Saltzman, and Y. Iwakiri. 2016. "Cellular Distribution of Injected PLGA-Nanoparticles in the Liver." *Nanomedicine : Nanotechnology, Biology, and Medicine* 12 (5): 1365–1374. doi:10.1016/j.nano.2016.01.013.
- Parrish, A. R., A. J. Gandolfi, and K. Brendel. 1995. "Precision-Cut Tissue Slices: Applications in Pharmacology and Toxicology." *Life Sciences* 57 (21): 1887–1901. doi:10.1016/0024-3205(95)02176-J.
- Riediker, M., D. Zink, W. Kreyling, G. Oberdörster, A. Elder, U. Graham, I. Lynch, et al. 2019. "Particle Toxicology and Health – Where Are we?" *Particle and Fibre Toxicology* 16 (1): 19. doi:10.1186/s12989-019-0302-8.
- Sauer, U. G., S. Vogel, A. Aumann, A. Hess, S. N. Kolle, L. Ma-Hock, W. Wohlleben, et al. 2014. "Applicability of Rat Precision-Cut Lung Slices in Evaluating Nanomaterial Cytotoxicity, Apoptosis, Oxidative Stress, and Inflammation." *Toxicology and Applied Pharmacology* 276 (1): 1–20. doi:10.1016/j.taap.2013.12.017.
- Schleh, C., M. Semmler-Behnke, J. Lipka, A. Wenk, S. Hirn, M. Schäffler, G. Schmid, U. Simon, and W. G. Kreyling. 2012. "Size and Surface Charge of Gold Nanoparticles Determine Absorption Across Intestinal Barriers and Accumulation in Secondary Target Organs after Oral Administration." *Nanotoxicology* 6 (1): 36–46. doi:10.3109/17435390.2011.552811.
- Shapero, K., F. Fenaroli, I. Lynch, D. C. Cottell, A. Salvati, and K. A. Dawson. 2011. "Time and Space Resolved Uptake Study of Silica Nanoparticles by Human Cells." *Molecular bioSystems* 7 (2): 371–378. doi:10.1039/c0mb00109k.
- Starokozhko, V., G. B. Abza, H. C. Maessen, M. T. Merema, F. Kuper, and G. M. M. Groothuis. 2015. "Viability, Function and Morphological Integrity of Precision-Cut Liver Slices During Prolonged Incubation: Effects of Culture Medium." *Toxicology In Vitro : An International Journal Published in Association with BIBRA* 30 (1 Pt B): 288–299. doi:10.1016/j.tiv.2015.10.008.
- Stribos, E. G. D., M. A. Seelen, H. van Goor, P. Olinga, and H. A. M. Mutsaers. 2017. "Murine Precision-Cut Kidney Slices as an Ex Vivo Model to Evaluate the Role of Transforming Growth Factor- β 1 Signaling in the Onset of Renal Fibrosis." *Frontiers in Physiology* 8: 1026. doi:10.3389/fphys.2017.01026.

- Thorley, A. J., P. Ruenraroengsak, T. E. Potter, and T. D. Tetley. 2014. "Critical Determinants of Uptake and Translocation of Nanoparticles by the Human Pulmonary Alveolar Epithelium." *ACS Nano* 8 (11): 11778–11789. doi:[10.1021/nn505399e](https://doi.org/10.1021/nn505399e).
- Tsoi, K. M., S. A. MacParland, X.-Z. Ma, V. N. Spetzler, J. Echeverri, B. Ouyang, S. M. Fadel, et al. 2016. "Mechanism of Hard-Nanomaterial Clearance by the Liver." *Nature Materials* 15 (11): 1212–1221. doi:[10.1038/nmat4718](https://doi.org/10.1038/nmat4718).
- Wang, F., M. G. Bexiga, S. Anguissola, P. Boya, J. C. Simpson, A. Salvati, and K. A. Dawson. 2013. "Time Resolved Study of Cell Death Mechanisms Induced by Amine-Modified Polystyrene Nanoparticles." *Nanoscale* 5 (22): 10868–10876. doi:[10.1039/c3nr03249c](https://doi.org/10.1039/c3nr03249c).
- Wick, P., S. Chortarea, O. T. Guenat, M. Roesslein, J. D. Stucki, S. Hirn, A. Petri-Fink, and B. Rothen-Rutishauser. 2015. "In Vitro-Ex Vivo Model Systems for Nanosafety Assessment." *European Journal of Nanomedicine* 7 (3). doi:[10.1515/ejnm-2014-0049](https://doi.org/10.1515/ejnm-2014-0049).
- Wilhelm, S., A. J. Tavares, Q. Dai, S. Ohta, J. Audet, H. F. Dvorak, and W. C. W. Chan. 2016. "Analysis of Nanoparticle Delivery to Tumours." *Nature Reviews Materials* 1 (5): 16014. doi:[10.1038/natrevmats.2016.14](https://doi.org/10.1038/natrevmats.2016.14).
- Xia, T., M. Kovochich, M. Liong, J. I. Zink, and A. E. Nel. 2008. "Cationic Polystyrene Nanosphere Toxicity Depends on Cell-Specific Endocytic and Mitochondrial Injury Pathways." *ACS Nano* 2 (1): 85–96. doi:[10.1021/nn700256c](https://doi.org/10.1021/nn700256c).